REGULAR PAPERS

In situ characterization of the film coverage and the charge transport in the alkylated-organic thin film transistor

Japanese Journal of Applied Physics **57**, 03EG14 (2018)
https://doi.org/10.7567/JJAP.57.03EG14

REGULAR PAPER

In situ characterization of the film coverage and the charge transport in the alkylated-organic thin film transistor

Takeshi Watanabe[1]*, Tomoyuki Koganezawa[1], Mamoru Kikuchi[2], Hiroki Muraoka[2], Satoshi Ogawa[2], Noriyuki Yoshimoto[2], and Ichiro Hirosawa[1]

[1]*Industrial Application Division, Japan Synchrotron Radiation Research Institute, Sayo, Hyogo 679-5198, Japan*
[2]*Graduate School of Engineering, Iwate University, Morioka 020-8551, Japan*

*E-mail: t5511001@spring8.or.jp

Received August 8, 2017; revised October 17, 2017; accepted November 6, 2017; published online February 16, 2018

We propose an in situ experimental method of investigating the correlations of the film coverage of the organic semiconductor layers and charge transport properties of organic thin film transistors during vacuum deposition. The coverage of each monolayer was estimated using the intensity of off-specular diffuse scattering and diffraction. Experimental data were obtained from the in situ measurements of two-dimensional grazing incidence X-ray scattering and charge transport. The source–drain current increased over the film coverage of the first monolayer (= 0.48). This is in agreement with the critical percolation coverage, indicating that the conductivities of the first and second monolayers are different.

1. Introduction

Organic thin film transistors (OTFTs) have attracted attention as new basic components of electronic devices. For practical application, it is important to ensure not only high field-effect mobility but also reliability under device-operating conditions. These device performances are strongly affected by surface morphology, grain size, crystal orientation, and polymorphism.[1–8] Therefore, crystallographic characterizations of the organic semiconductor layer are necessary for optimizing the performance of OTFTs.

The in situ characterization of the morphology and/or charge transport of OTFT is an appropriate approach to understanding the process of thin film growth and the carrier transport mechanism. Many reports have been published studying thin film growth and/or carrier transport using in situ experimental methods.[9–16] However, there has been no simultaneous characterization of the morphologies and transport property of OTFTs.

We have recently developed a powerful instrumentation that enables in situ two-dimensional grazing incidence X-ray scattering (2D-GIXS) and electrical current measurements of OTFTs during vacuum deposition.[16–18] In the current study, we focused on the correlations of film coverage and charge transport of alkylated OTFTs. Alkylated molecular thin films have been widely used in OTFT materials to control physical properties such as solubility, environmental stability, and mobility since the substitution of organic semiconductors with alkyl chains is a simple approach.[19–24] In this paper, we propose a method of investigating the correlations of film coverage and charge transport by in situ observations of the source–drain current (I_{ds}) and 2D-GIXS. We estimated the film coverage of each monolayer (ML) using the intensity of off-specular diffuse scattering and diffraction. We also discuss the correlation of film coverage and charge transfer on OTFTs.

2. Experimental methods

We fabricated OTFTs with a bottom-contact structure. A highly p-doped silicon wafer (gate electrodes) was used as a substrate covered with source and drain electrodes above the thermal silicon dioxide (insulator, 300 nm in thickness). Au

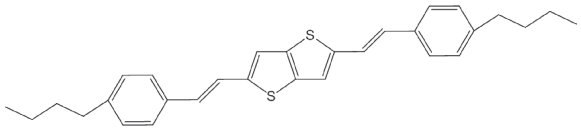

Fig. 1. Molecular structure of DH-DSTT.

was deposited as source and drain electrodes (channel length: $L = 1$ mm, channel width: $W = 10$ mm) on top of the substrate through a shadow mask. The alkylated organic semiconducting material α,ω-hexyl-distyryl thieno thiophene (DH-DSTT, see the molecular structure in Fig. 1) was vacuum deposited on the substrate. DH-DSTT was synthesized in a previous study.[25] The vacuum pressures during deposition of the organic layer and metal electrodes were 2.0×10^{-4} and 1.4×10^{-5} Pa, respectively. The deposition rate was monitored using a crystal quartz microbalance and maintained at a constant value of 0.03 nm/min. The deposition rate was calibrated through ex situ atomic force microscopy (AFM) in air. The total deposition time was 6600 s.

In situ observations of the 2D-GIXS profile and charge transport of the DH-DSTT thin film were conducted at BL19B2 in SPring-8. The X-ray energy in this experiment was 12.40 keV. The X-ray beam was formed by a four quadrant slit into horizontal and vertical widths of 0.2 mm. The incident X-rays impinged on the channel between the source and drain electrodes as shown in Fig. 2. The grazing angle of the X-ray was set to $\omega = 0.12°$. The scattered profile from the organic thin film was detected using an area detector (PILATUS 300K).[26] The distance between the sample and the detector was 174.2 mm, which was calibrated by observing the diffraction patterns of the lanthanum hexaboride powders. The charge transport was measured in vacuum with Keithley 2400 and 6517A electrometers. The drain–source voltage (V_{ds}) and gate–source voltage (V_{gs}) were maintained at −60.0 and −80.0 V, respectively, throughout the in situ experiment.

3. Results and discussion

3.1 AFM measurements

The surface morphology, obtained through AFM, is shown in

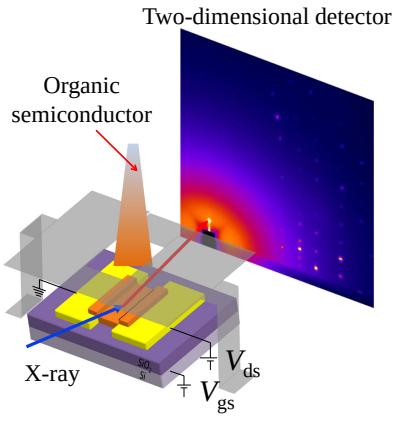

Fig. 2. (Color online) Schematic illustration of 2D-GIXS measurement setup.

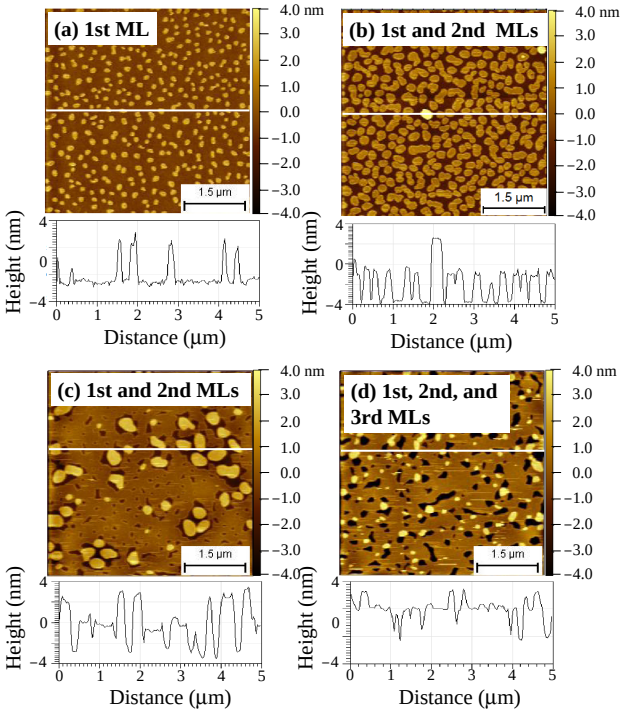

Fig. 3. (Color online) AFM images of DH-DSTT thin film morphologies for increasing film coverage. (a) First ML. (b), (c) First and second MLs. (d) First, second, and third MLs.

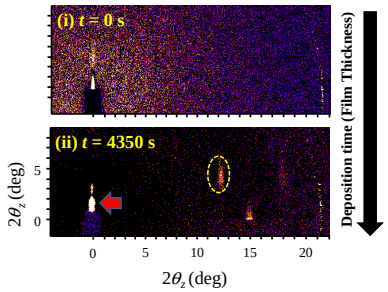

Fig. 4. (Color online) Observed 2D-GIXS patterns during vacuum deposition of DH-DSTT thin film (i) $t = 0$ s, (ii) $t = 4350$ s. 2D-GIXS images were subtracted using first frame of time series to discriminate slight change in scattering patterns.

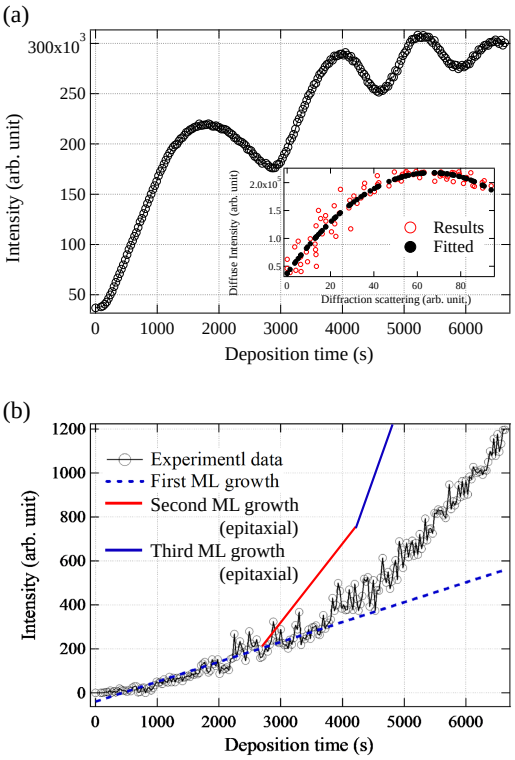

Fig. 5. (Color online) Intensity of (a) off-specular diffuse scattering and (b) peak intensity of diffraction as function of deposition time. Inset of (a): experimental results of intensity of off-specular diffuse scattering as function of peak intensity of diffraction at first ML.

Fig. 3. The DH-DSTT molecules nucleated at the substrate surface when the deposition started. These islands grew laterally, and the average grain size became 333 nm. The first ML was almost covered and the second ML was newly nucleated with increasing film thickness. The third ML appeared above the second ML before the second ML was covered completely.

3.2 In situ X-ray scattering measurements

The 2D-GIXS patterns before and after deposition of the DH-DSTT thin film are shown in Fig. 4. The $2\theta_z$ on the vertical axis and $2\theta_{xy}$ on the horizontal one denote the take-off and horizontal components of the scattering angle, respectively. Off-specular diffuse scattering from the substrate along the $2\theta_z$ axis at $2\theta_{xy} = 0°$ was observed before deposition. At $t = 4350$ s, off-specular diffuse scattering from DH-DSTT (red arrow in Fig. 4) and three diffraction rods newly appeared at $2\theta_{xy} = 12.3$, 14.9, and 18.0°. Figures 5(a) and 5(b) show the intensity of the off-specular diffuse scattering at $2\theta_z = 0.9°$ and the peak intensity of diffraction (yellow circle in Fig. 4) as a function of deposition time. The periodical oscillations of the off-specular diffuse scattering are shown in Fig. 5(a). Off-specular diffuse scattering is known to be caused by surface roughness.[27] These results indicate that the surface roughness of DH-DSTT thin films periodically changes. The amplitude of the off-specular diffuse scattering was also found to decrease with deposition time. The peak intensity of diffraction, on the other hand, increased monotonically, as shown in Fig. 5(b).

3.3 Estimations of film coverage

We estimated the film coverage of each ML using the intensity of the off-specular scattering along the $2\theta_z$ axis and peak intensity of the diffraction obtained from the in situ 2D-GIXS measurement. The coverage was defined as the area exposed for the surface of each layer as shown in Fig. 6(a).

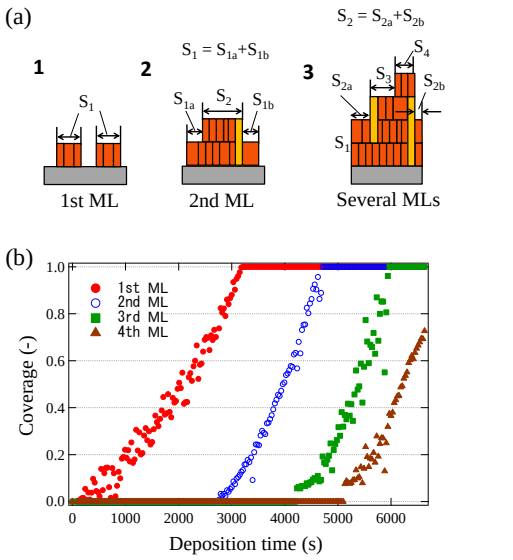

Fig. 6. (Color online) (a) Schematic illustration of growth mode of DH-DSTT film. (b) Estimated film coverages of DH-DSTT thin film.

3.3.1 First ML. Figure 6(a) **1** shows a schematic illustration of the DH-DSTT thin film at the first ML. The peak intensity of the diffraction at this ML increased linearly and was proportional to the film coverage. This peak intensity I_1 can be written as

$$I_1 = CS_1, \tag{1}$$

where C is constant. The intensity of the off-specular diffuse scattering was proportional to the variance of the height: $\sigma^2 = \langle h^2 \rangle - \langle h \rangle^2$, where h is the height of the actual surface.[27] h was estimated to be 3.29 nm using the observed AFM data. The off-specular diffuse scattering coming from the DH-DSTT thin film can be denoted as $AS_1(1 - S_1)$, where A is a constant value and S_1 is the film coverage of the first ML. At the first ML, the off-specular diffuse scattering from the substrate should be considered as shown in Fig. 6(a) **1**. The off-specular diffuse scattering coming from the substrate can be denoted as $B(1 - S_1)$, where B is a constant value. The intensity of the off-specular diffuse scattering at the first ML D_1 can be written as

$$D_1 = AS_1(1 - S_1) + B(1 - S_1). \tag{2}$$

Thus, the intensity of the off-specular diffuse scattering should be related to peak intensity of diffraction with a parabolic function. The inset in Fig. 5(a) shows the experimental results of the off-specular diffuse-scattering intensity as a function of diffraction intensity. Good agreement was found between our calculation with a parabolic function and the observed profiles, and a correlation coefficient of $R = 0.92$ is obtained.

When the thin film exhibited perfect layer-by-layer growth, Eqs. (1) and (2) suggest that the intensity of the off-specular diffuse scattering should be periodic and zero for the film covered completely ($S_1 = 1.0$). However, the observed off-specular diffuse scattering during deposition was not zero, but increased periodically with a local minimum, as shown in Fig. 5(a). This indicates that the nucleation of the second ML started before the first ML was covered completely. The growth mode was in good agreement with the results of the AFM.

3.3.2 Second ML. Figure 6(a) **2** shows schematic illustrations of the DH-DSTT thin film at the second ML. If the DH-DSTT thin film grows epitaxially along the stacking direction, the peak intensity of the diffraction is proportional to $4S_2 + S_1$ (S_2 is the coverage of the second ML). In this case, the gradient of the peak intensity increases as shown in the red line of Fig. 5(b). However, the gradient estimated from the experimental data in all regions was found to be smaller than that shown by the red line as shown in Fig. 5(b). Therefore, the DH-DSTT thin film formed nonepitaxial layers along the stacking direction. The peak intensity is divided into two terms: epitaxial and nonepitaxial grows. This peak intensity I_2 is expressed as

$$I_2 = C\{[rL_{(2)} + 2(1 - r)]S_2 + S_1\}, \tag{3}$$

where r and $L_{(2)}$ are the ratio of epitaxial growth with the first ML and the Laue function, respectively. r was calculated to be 0.08 from the experimental data. The disorder in the stacking direction at the initial few MLs has been reported in Refs. 28 and 29. The intensity of the off-specular diffuse scattering at the second ML, D_2, can be calculated similarly to that at the first ML as

$$D_2 = A[(S_1 + 4S_2) - (S_1 + 2S_2)^2] + B(1 - S_1 - S_2). \tag{4}$$

3.3.3 Several MLs. Figure 6(a) **3** shows a schematic illustration of the DH-DSTT thin film at several MLs. At these MLs, we made three additional assumptions. The first assumption was that the nth ML ($N \geq 3$) was epitaxially grown when the $(n - 1)$th ML was grown epitaxially. The second assumption was that the nth ML was grown epitaxially at a rate of $r = 0.08$. If the DH-DSTT thin film grows epitaxially above the three MLs, the peak intensity should increase by Laue function as shown by the blue line in Fig. 5(b). Therefore, we assumed that the epitaxial rate was small. The third assumption was that

$$\sum_{n=N-2}^{N} S_n = 1 \quad (N \geq 3). \tag{5}$$

The intensity of the off-specular diffuse scattering and the peak intensity of diffraction can be calculated similarly to those of the second ML.

Figure 6(b) shows the results of the film coverage of each ML estimated using the intensity of diffraction and off-specular diffuse scattering. The DH-DSTT film was found to form four MLs in this experiment. The growth of the second ML started at $S_1 = 0.73$. On the other hand, the growth of the third and fourth MLs respectively started at $S_2 = 0.55$ and $S_3 = 0.37$. These results indicate layer-growth behavior at the first and second MLs and island growth behavior after the deposition of three MLs. We also found that the time it takes to completely cover each layer (τ_n) decreases depending on the number of layers. The τ_n values are respectively $\tau_1 = 3150$ s (first ML), $\tau_2 = 2010$ s (second ML), and $\tau_3 = 1920$ s (third ML). Note that τ_1 was 1.6 and 1.7 times larger than τ_2 and τ_3, which implies that the thin film growth rate at the DH-DSTT film surface was higher than at the SiO_2 surface.

3.4 Correlations of charge transport and film coverage

Figure 7(a) shows the off-specular diffuse scattering and I_{ds} during deposition as a function of deposition time. I_{ds} increased markedly as film thickness increased over deposi-

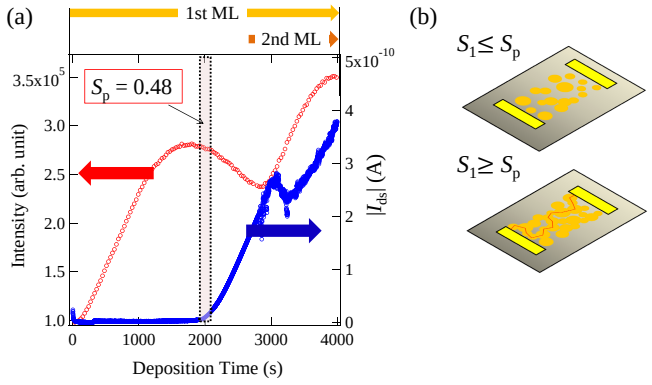

Fig. 7. (Color online) (a) Off-specular diffuse scattering intensity and I_{ds} during deposition as function of deposition time. (b) Schematic depicting carrier transport before and after critical percolation coverage.

tion time $t = 1920$ s. The DH-DSTT shows typical p-type OTFT characteristics. Compared with the off-state ($I_{ds} \cong 9.4 \times 10^{-13}$ A), I_{ds} under $V_{ds} = -60$ V and $V_{gs} = -80$ V was amplified to $I_{ds} \cong 1.0 \times 10^{-10}$ A after $t = 1920$ s. Therefore, the data after $t = 1920$ s were in an on-state current. The onset of I_{ds} was approximately equal to the time exhibiting the local maximum value of the off-specular diffuse scattering. I_{ds} increased markedly with the film coverage of the first ML: $S_p = 0.48$. The obtained S_p was in agreements with the critical percolation coverage proposed by Smith et al.[30] The same tendency was reported by many groups.[7,10,11] A schematic depicting the process of carrier transport after percolation is also shown in Fig. 7(b). I_{ds} was also observed to exhibit the local maximum values at $t = 3000$ s. While maintaining thin film growth, the intensity of off-specular diffuse scattering and I_{ds} increased again. Muck et al. reported a significant decrease in the field-effect mobility after the start of the second ML using alkylated thiophene molecules.[11] This is considered the trap state introduced by island boundary and/or crystal defects. However, we could not ascertain the origins of this decrease in this experiment. Note that $|\Delta I_{ds}|/\Delta t$ beyond $t = 3000$ s slightly decreased compared with that in the first period (t =1920–3000 s).

4. Conclusions

We proposed an in situ experimental method of investigating the correlations of the film coverage of the organic semiconductor layer and transport during vacuum deposition. We succeeded in measuring X-ray scattering and charge transport during vacuum deposition. We also estimated the film coverage of each ML using the intensity of off-specular diffuse scattering along the $2\theta_z$ axis and peak intensity of the diffraction obtained from in situ 2D-GIXS measurement. I_{ds} increased markedly with the film coverage of the first ML; $S_p = 0.48$. The obtained S_p was in agreement with the percolation threshold value. $|\Delta I_{ds}|/\Delta t$ beyond $t = 3000$ s slightly decreased compared with that in the first period.

Acknowledgments

The authors would like to thank Atsufumi Kumagai, Toshinori Tanisawa, and Kousaku Nishida of Iwate University for their insightful advice. The synchrotron radiation experiments were conducted at BL19B2 in SPring-8 with the approval of JASRI (Proposal Nos. 2011B0036 and 2013A0036).

1) Y. Ueda, M. Watanabe, and H. Yamaguchi, Mol. Cryst. Liq. Cryst. **267**, 175 (1995).
2) B. Servet, G. Horowitz, S. Ries, O. Lagorsse, P. Alnot, A. Yassar, F. Deloffre, P. Srivastava, R. Hajlaoui, P. Lang, and F. Garnier, Chem. Mater. **6**, 1809 (1994).
3) S. Furukawa, Thin Solid Films **331**, 222 (1998).
4) G. Horowitz and M. E. Hajlaoui, Synth. Met. **122**, 185 (2001).
5) Y.-Y. Noh, J.-J. Kim, Y. Yoshida, and K. Yase, Adv. Mater. **15**, 699 (2003).
6) H. Yanagisawa, T. Tamaki, M. Nakamura, and K. Kudo, Thin Solid Films **464–465**, 398 (2004).
7) R. Ruiz, A. Papadimitratos, A. C. Mayer, and G. Malliaras, Adv. Mater. **17**, 1795 (2005).
8) K. Fukao, T. Horiuchi, and K. Matsushige, Thin Solid Films **171**, 359 (1989).
9) E. M. Mannebach, J. W. Spalenka, P. S. Johnson, Z. Cai, F. J. Himpsel, and G. Evans, Adv. Mater. **23**, 554 (2013).
10) M. Kiguchi, M. Nakayama, K. Fujiwara, K. Ueno, T. Shimada, and K. Saiki, Jpn. J. Appl. Phys. **42**, L1408 (2003).
11) T. Muck, V. Wagner, M. Leufgen, J. Geurts, and L. W. Molenkamp, Synth. Met. **146**, 317 (2004).
12) A. C. Mayer, R. Ruiz, R. L. Headrick, A. Kazimirov, and G. G. Malliaras, Org. Electron. **5**, 257 (2004).
13) S. Kowarik, A. Gerlach, W. Leitenberger, J. Hu, G. Witte, C. Wöll, U. Pietsch, and F. Schreiber, Thin Solid Films **515**, 5606 (2007).
14) Y. Tsuruma, A. Al-Mahboob, S. Ikeda, J. T. Sadowski, G. Yoshikawa, Y. Fujikawa, T. Sakurai, and K. Saiki, Adv. Mater. **21**, 4996 (2009).
15) A. Kubono, Y. Minagawa, and T. Ito, Jpn. J. Appl. Phys. **48**, 020211 (2009).
16) T. Watanabe, T. Hosokai, T. Koganezawa, and N. Yoshimoto, Mol. Cryst. Liq. Cryst. **566**, 18 (2012).
17) T. Watanabe, M. Kikuchi, K. Nishida, T. Koganezawa, N. Yoshimoto, and I. Hirosawa, Mol. Cryst. Liq. Cryst. **636**, 168 (2016).
18) T. Watanabe, T. Koganezawa, M. Kikuchi, C. Videlot-Ackermann, J. Ackermann, H. Brisset, N. Yoshimoto, and I. Hirosawa, J. Cryst. Growth **468**, 816 (2017).
19) H. Ebata, T. Izawa, E. Miyazaki, K. Takimiya, M. Ikeda, H. Kuwabara, and T. Yui, J. Am. Chem. Soc. **129**, 15732 (2007).
20) T. J. Shin, H. Yang, M.-M. Ling, J. Locklin, L. Yang, B. Lee, M. E. Roberts, A. B. Mallik, and Z. Bao, Chem. Mater. **19**, 5882 (2007).
21) C. Videlot-Ackermann, H. Brisset, J. Ackermann, J. Zhang, P. Raynal, F. Fages, G. H. Mehl, T. Tnanisawa, and N. Yoshimoto, Org. Electron. **9**, 591 (2008).
22) M. J. Kang, I. Doi, H. Mori, E. Miyazaki, K. Takimiya, M. Ikeda, and H. Kuwabara, Adv. Mater. **23**, 1222 (2011).
23) Y. Yuan, G. Giri, A. L. Ayzner, A. P. Zoombelt, S. C. B. Mannsfeld, J. Chen, D. Nordlund, M. F. Toney, J. Huang, and Z. Bao, Nat. Commun. **5**, 3005 (2014).
24) H. Okamoto, S. Hamao, H. Goto, Y. Sakai, M. Izumi, S. Gohda, Y. Kubozono, and R. Eguchi, Sci. Rep. **4**, 5048 (2014).
25) H. Ito, T. Yamamoto, N. Yoshimoto, N. Tsushima, H. Muraoka, and S. Ogawa, Heteroatom Chem. **24**, 25 (2013).
26) H. Toyokawa, M. Suzuki, C. Brönnimann, E. F. Eikenberry, B. Henrich, G. Hülsen, and P. Kraft, AIP Conf. Proc. **879**, 1141 (2007).
27) S. K. Sinha, E. B. Sirota, S. Garoff, and H. B. Stanley, Phys. Rev. B **38**, 2297 (1988).
28) R. Hayakawa, A. Turak, X. Zhang, N. Hiroshiba, H. Dosch, T. Chikyow, and Y. Wakayama, J. Chem. Phys. **133**, 034706 (2010).
29) A. Moser, I. Salzmann, M. Oehzelt, A. Neuhold, H. G. Flesch, J. Ivanco, S. Pop, T. Toader, D. R. T. Zahn, D. M. Smilgies, and R. Resel, Chem. Phys. Lett. **574**, 51 (2013).
30) L. N. Smith and C. J. Lobb, Phys. Rev. B **20**, 3653 (1979).